fishes

MDPI

Article

Numerical Investigation of Flow Regulation Using a Skew Branch Pipe in Aquaculture Vessel Pipeline Systems

Wenyun Huang [1,2,3], Suoxian Yang [1,2], Weitang Wang [4], Liang Wang [1,2] and Ruosi Zha [5,*]

[1] Fishery Machinery and Instrument Research Institute, Chinese Academy of Fishery Science, Shanghai 200092, China; huangwenyun@fmiri.ac.cn (W.H.); yangsuoxian@fmiri.ac.cn (S.Y.); wangliang@fmiri.ac.cn (L.W.)
[2] Key Laboratory of Ocean Fishing Vessel and Equipment, Ministry of Agriculture, Shanghai 200092, China
[3] East China Sea Fisheries Research Institute, Shanghai 200090, China
[4] China State Shipbuilding Corporation Qingdao Beihai Shipbuilding Co., Ltd., Qingdao 266520, China; wwt204@126.com
[5] School of Ocean Engineering and Technology, Sun Yat-sen University & Southern Marine Science and Engineering, Guangdong Laboratory (Zhuhai), Zhuhai 519082, China
* Correspondence: zhars@mail.sysu.edu.cn

Abstract

Guoxin No. 1, one of the largest smart aquaculture vessels currently in operation, represents an important development in large-scale mobile aquaculture platforms. Continuous circulation of oxygen-rich seawater is essential for maintaining suitable culture conditions in intensive aquaculture vessels. However, the complex pipeline arrangements used for distributing seawater among multiple farming tanks can result in uneven flow allocation. In this study, three-dimensional CFD simulations were conducted to investigate the internal flow behaviors and flow distribution in a T-type pipeline system for an aquaculture vessel. Extending previous studies based on coplanar branch configurations, a non-coplanar skew branch pipe arranged in the xy-plane was investigated. Particular attention was given to the influence of the spatial offset between the branch pipe and the main pipeline axis on velocity distribution, pressure variation, and outlet flow rates. The results show that the spatial offset modifies the momentum transfer process at the junction and generates a swirling motion inside the main pipeline. Compared with the conventional inclined branch configuration, the offset branch shifts the high-velocity core away from the pipe center and reduces the imbalance between the two outlet flow rates. The pressure field is also redistributed due to the asymmetric momentum injection, indicating a trade-off between improved flow uniformity and local pressure variation. The present study demonstrates the potential of non-coplanar skew branch configurations as a passive approach for improving seawater distribution in large-scale aquaculture vessel pipeline systems.

Keywords: aquaculture vessel; internal flow; flow rate control; computational fluid dynamics

Key Contribution: This study proposes a novel flow control strategy for aquaculture vessels by introducing a non-coplanar branch pipe configuration with a spatial center offset. This geometric analysis provides a theoretical foundation for improving water exchange efficiency in large-scale marine farming tanks.

Check for updates

Academic Editors: Changtao Guan, Gang Wang and Yuyan Li

Received: 18 August 2026
Revised: 25 September 2026
Accepted: 10 October 2026
Published: 15 October 2026

Copyright: © 2026 by the authors. Licensee MDPI, Basel, Switzerland. This article is an open access article distributed under the terms and conditions of the Creative Commons Attribution (CC BY) license.

1. Introduction

Aquaculture has become an important contributor to global aquatic food production as demand for seafood continues to rise and capture fisheries approach their production

limits [1]. At the same time, conventional coastal aquaculture is increasingly constrained by limited space, environmental impacts, disease risks, and competition for coastal resources [2]. These constraints have encouraged the development of offshore systems, where fish welfare, containment design, and exposure to waves and currents become central engineering considerations [3,4]. Recent numerical and experimental studies of vessel-shaped and submersible farms, as well as sloshing in aquaculture vessels, further illustrate the hydrodynamic demands placed on large offshore facilities [5–8]. Smart-farm concepts also emphasize the need to integrate water circulation, aeration, monitoring, and control within a single production system [9].

Unlike conventional cage-based systems, aquaculture vessels combine culture tanks, seawater pipelines, oxygen-supply equipment, and automated management systems within a confined onboard space. Their operation therefore depends strongly on the reliability of the internal water-distribution network. Guoxin No. 1 is a representative example: multiple culture tanks are connected to an extensive seawater circulation system, and a single pump may serve more than one tank through a flow-diversion pipeline [10]. Previous work on smart-farm pumping and model-assisted pump control has shown that hydraulic regulation is closely linked to energy use and operational stability [11,12].

A balanced flow allocation among farming tanks is required because water exchange affects oxygen availability, waste removal, and the stability of the culture environment. Tank-scale studies have shown that inlet arrangement, tank geometry, circulation pattern, and residence time influence both hydraulic performance and fish distribution [13–15]. Related work on recirculating aquaculture systems, biofloc facilities, land-based production, and shellfish installations has likewise shown that infrastructure and operating conditions shape the local culture environment [16–19]. The cultured fish themselves may also modify the surrounding flow field, particularly at high stocking densities [20]. These findings support the need to consider the hydraulic behaviour of the upstream pipeline network, rather than treating each farming tank as an isolated unit.

Branch pipelines and T-junctions are widely used to divide and redirect fluid flow. Their internal flow behaviour depends on junction geometry, inlet conditions, Reynolds number, and the resulting pressure field. Flow separation, recirculation, secondary motion, and asymmetric velocity profiles commonly develop near the junction. Costa et al. [21] showed that edge geometry in a 90° tee changes both the local flow structure and the associated losses. Han et al. [22] later examined three-dimensional flow in blind-tee pipes and likewise found that relatively small geometric changes can alter the development of the junction flow.

Computational fluid dynamics (CFD) has been widely used to examine flow fields that are difficult to resolve experimentally in aquaculture facilities. For example, Oca et al. [13] assessed the effect of inlet configuration in rectangular tanks, while Xue et al. [23] coupled CFD with particle tracking to study pollutant transport. Li et al. [24] extended this approach to a rearing tank aboard an aquaculture vessel. By contrast, relatively few studies have addressed flow regulation within the vessel pipeline itself. Huang and Zha [10] investigated a coplanar branch inlet in a T-type pipeline and showed that gravity, branch-flow rate, and installation angle can change the discharge split between two outlets. That work established the feasibility of geometry-assisted flow regulation, but the branch axis still intersected the central axis of the main pipe.

In practical offshore engineering applications, pipeline layouts are frequently restricted by limited installation space and complex equipment arrangements. Depending on installation constraints, a non-coplanar branch may be considered as an alternative arrangement. Compared with traditional coplanar branches, skew branch pipes introduce additional spatial degrees of freedom, which may generate tangential momentum and induce swirling

flow within the main pipeline. Such swirling structures have potential advantages for enhancing mixing performance, modifying pressure distribution, and improving downstream flow uniformity. However, the influence of spatial offset and skewed branch geometry on internal flow characteristics and outlet flow balance in aquaculture vessel pipelines remains unclear.

In the present study, a T-type pipeline system for a large-scale aquaculture vessel is investigated, as illustrated in Figure 1. The pipeline system consists of a main inlet pipe connected to a pump system, a branch inlet pipe for flow regulation, and two outlet pipes supplying seawater to different aquaculture tanks. The flow rates at the main inlet, branch inlet, upper outlet, and lower outlet are defined as Q_1, Q, Q_2, and Q_3, respectively. In the conventional configuration, the branch pipe is located within the same plane as the main pipeline, which may generate asymmetric flow distribution due to complex momentum exchange and pressure redistribution inside the junction region. To overcome this limitation, this study introduces a skew branch pipe configuration with a spatial center offset, aiming to generate controlled swirling flow and improve the balance of outlet flow rates.

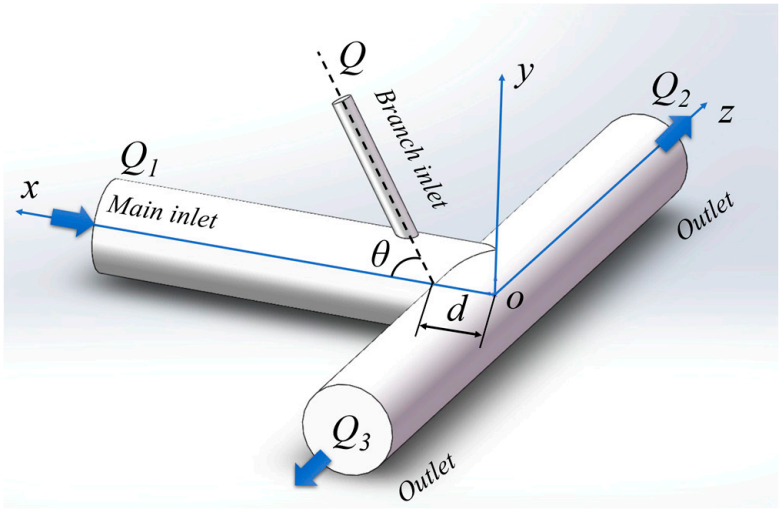


Figure 1. The T-type pipeline system with a main inlet, skew branch inlet, and two outlet pipes for flow regulation in an aquaculture vessel.

Therefore, the present study aims to investigate the effects of a skew branch pipe on flow distribution and internal flow characteristics in a T-type pipeline system for an aquaculture vessel. A three-dimensional CFD framework was established to quantify the influence of branch inclination angle and spatial center offset on velocity fields, pressure distribution, and outlet flow rates. By introducing a non-coplanar branch configuration, this study aims to develop an effective passive flow-control strategy for improving seawater distribution among multiple farming tanks and providing theoretical support for the hydraulic design of large-scale smart aquaculture vessels.

The remainder of this paper is organized as follows. Section 2 presents the numerical methodology, including the governing equations, turbulence model, spatial discretization method, and computational settings. Section 3 describes the computational geometries, mesh generation strategy, boundary conditions, and simulation cases for different skew branch configurations. Section 4 discusses the numerical results, including grid independence verification, velocity field characteristics, flow-rate distribution, pressure variation, and the influence of branch geometry on internal flow behaviors. Finally, Section 5 summarizes the main conclusions and discusses the engineering implications of applying skew branch pipes for flow regulation in offshore aquaculture vessel systems.

2. Numerical Methods

2.1. Governing Equations

The internal flow within the T-type pipeline system is modeled as an incompressible viscous fluid. The fundamental physical behavior is governed by the Reynolds-Averaged Navier–Stokes (RANS) equations [25,26]. These include the continuity equation for mass conservation and the momentum equations, which are expressed as follows

$$\frac{\partial \rho}{\partial t} + \nabla \cdot \left(\rho \overline{V}\right) = 0 \tag{1}$$

$$\frac{\partial}{\partial t}\left(\rho \overline{V}\right) + \nabla \cdot \left(\rho \overline{V} \bigotimes \overline{V}\right) = -\nabla \cdot \overline{p} I + \nabla \cdot \left(\overline{\tau} + \tau_{RANS}\right) + f_b \tag{2}$$

where ρ is the density of fluid, $\overline{V}$ is the average velocity, $\overline{p}$ is the average pressure, I is the unit tensor, f_b is the resultant body force, $\overline{\tau}$ is the average viscous stress tensor. The additional stress tensor τ_{RANS} is calculated by:

$$\tau_{RANS} = 2\mu_t S - 2/3\left(\mu_t \nabla \cdot \overline{V}\right) I \tag{3}$$

in which S is the mean strain rate tensor. The eddy viscosity, μ_t, is defined as:

$$\mu_t = \rho k T \tag{4}$$

where k is the kinetic energy and T is equaling to α^*/ω, in which α^* is a coefficient and ω is the specific dissipation rate.

2.2. Turbulence Modeling

The shear-stress-transport (SST) k–ω model was used to close the RANS equations. This model blends the near-wall behaviour of the k–ω formulation with the free-stream characteristics of the k–ε formulation and is well suited to flows involving adverse pressure gradients and separation [27]. More computationally intensive hybrid RANS–LES methods and data-informed turbulence closures have been developed for complex turbulent flows [28,29]; however, the SST k–ω model was selected here to retain a practical balance between near-wall resolution and computational cost. Its transport equations are given below.

$$\frac{\partial(\rho k)}{\partial t} + \nabla \cdot \left(\rho k \overline{V}\right) = P_k + \nabla[(\mu + \sigma_k \mu_t)\nabla k] - \beta^* \rho k \omega \tag{5}$$

$$\begin{gathered}\frac{\partial(\rho|\omega)}{\partial t} + \nabla \cdot \left(\rho \omega \overline{V}\right) = P_\omega - \beta \rho \omega^2 + \nabla[(\mu + \sigma_\omega \mu_t)\nabla \omega] \\ +2(1 - F_1)\frac{\rho \sigma_d}{\omega} \nabla \cdot k \nabla \cdot \omega\end{gathered} \tag{6}$$

where β is the thermal expansion coefficient, μ is the dynamic viscosity, σ_k, σ_ω and σ_d are coefficients, F_1 is a blend function, and P_k and P_ω are the production terms calculated by the equation:

$$P_k = P_\omega k/\gamma \omega \tag{7}$$

2.3. Finite-Volume Discretization

The numerical simulations were conducted using STAR-CCM+. In this work, the finite-volume method is adopted to discretize the governing partial differential equations [30]. Body-fitted mesh techniques are utilized to resolve complex geometric configurations. The discretized convective term evaluated at cell faces can be expressed as:

$$(\phi \rho \boldsymbol{v} \cdot \boldsymbol{a})_f = \left(\dot{m}\phi\right)_f = \dot{m}_f \phi_f \tag{8}$$

where ϕ_f represents an arbitrary flow variable and $\dot{m}_f$ denotes the mass flow rate at a grid cell face. The convective flux is evaluated using the second-order upwind (SOU) scheme, as formulated in Equation (9).

$$(\dot{m}\phi)_f = \begin{cases} \phi_0 + (\boldsymbol{x}_f - \boldsymbol{x}_0) \cdot (\nabla\phi)_{r,0} & \dot{m}_f \geq 0 \\ \phi_1 + (\boldsymbol{x}_f - \boldsymbol{x}_1) \cdot (\nabla\phi)_{r,1} & \dot{m}_f < 0 \end{cases} \quad (9)$$

Meanwhile, the diffusive flux across interior cell faces is discretized according to Equation (10):

$$D_f = (\Gamma \nabla\phi \cdot \boldsymbol{a})_f \quad (10)$$

in which Γ denotes the diffusivity defined at the cell face.

In this work, temporal discretization was performed using a second-order implicit unsteady scheme to capture the transient behavior of the flow, as evidenced by the time-history oscillations observed in the velocity and pressure probes. The time step was selected to maintain a global Courant-Friedrichs-Lewy (CFL) number within stable limits, ensuring that the temporal evolution of mass flow rates and the internal pressure field reached a statistically steady state. In this study, CFL = 1.0 was applied. Pressure-velocity coupling was managed through the SIMPLE (Semi-Implicit Method for Pressure-Linked Equations) algorithm to ensure efficient convergence during each time step.

3. Geometries and Grids Generation

The inlet and outlet pipelines have a length L = 3 m, while their diameters satisfy $\phi_1 = \phi_2 = \phi_3$ = 0.7 m. The primary geometry is based on a flow diverter, which is composed of one main inlet pipe and two outlet pipes. The modified T-type pipeline is fitted with an extra branch pipe dedicated to flow regulation. The branch pipe has a diameter of ϕ = 0.15 m. These parameters are taken from the original design by Huang and Zha [10]. The density of sea water is 1024.7 kg/m^3, dynamic viscosity is 0.00105 Pa·s at 20 °C.

Distinct from previous coplanar designs [10], the special branch pipe is oriented in the *xy*-plane, perpendicular to the *z*-axis but skewed relative to the main inlet axis. A critical new parameter, the center offset, *d*, is introduced, defined as the perpendicular distance from the central axis of the main pipe to the central axis of the branch pipe in the *xy*-plane.

To systematically evaluate the impact of these parameters on flow distribution, three specific cases/geometries were modeled, as shown in Figure 2. For Figure 2a, this configuration serves as the baseline model, representing a standard T-pipe junction. In this case, the inclusion angle is set at a perpendicular, 90°, and the center offset is zero, meaning the longitudinal axis of the branch inlet directly intersects the central axis of the main pipe. From a fluid dynamics perspective, this layout results in a direct impingement of the branch flow onto the opposing inner wall of the main pipe. This typically creates a high-pressure stagnation zone and symmetric flow separation but notably lacks any induced tangential velocity or rotational flow component. In terms of Figure 2b, the branch pipe is tilted to an acute inclusion angle of 45° while maintaining a zero center offset d = 0. Although the axes of the branch and the main pipe still reside within the same geometric plane and intersect at a common origin, the inclination alters the axial momentum distribution. This configuration is designed to investigate how a streamlined entry angle, without eccentricity, affects the mass flow ratio between the upper and lower outlets. Figure 2c represents the core innovative configuration of this study—the inclined skew junction with a given offset. Here, the 45° inclusion angle is maintained, but a significant spatial center offset of d = 0.5 m is introduced. In this non-coplanar arrangement, the branch axis is intentionally shifted away from the main pipe's central axis. As the fluid enters from the branch inlet, this offset allows the flow to be injected tangentially into the main pipe's cross-section

rather than directly toward its center. This tangential momentum injection is hypothesized to induce a swirling flow and vortex that propagates downstream. Such a mechanism is strategically utilized to redistribute the internal pressure field and equalize the mass flow rates between the two outlets, addressing the inherent hydraulic imbalances in asymmetric vessel piping systems.

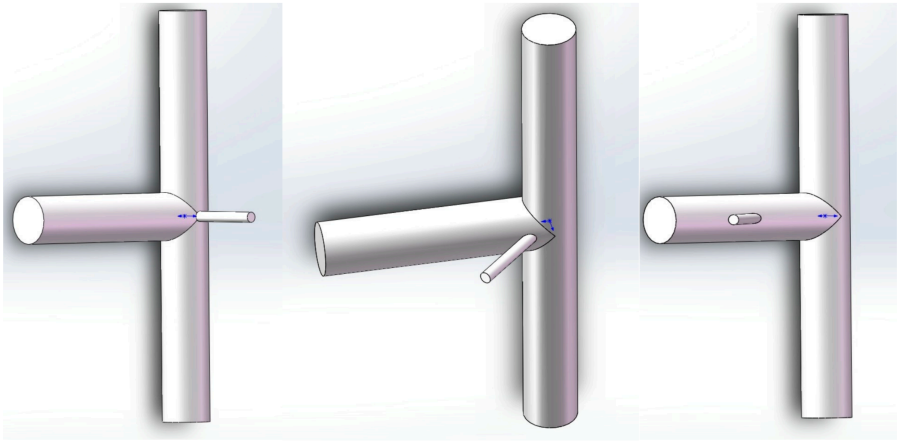


Figure 2. The T-type pipe models with different settings of the skew branch pipe (* is the original point): (**a**) $\theta = 90°$ and $d = 0$ m; (**b**) $\theta = 45°$ and $d = 0$ m; (**c**) $\theta = 45°$ and $d = 0.5$ m.

For grids generation, a polyhedral meshing model was taken advantage of in the STAR-CCM+ solver. The selection of polyhedral cells over traditional tetrahedral or hexahedral grids was driven by several numerical considerations. In simulations involving swirling flows, the flow direction is frequently non-aligned with the mesh. Traditional hexahedral or trimmed-cell meshes are prone to significant numerical diffusion when the flow crosses cell faces at skewed angles. Polyhedral cells, with their more isotropic shape, are inherently more robust, ensuring that the swirling momentum is preserved as it propagates downstream. While structured hexahedral meshes (O-grids) offer high efficiency for simple cylinders, they are notoriously difficult to implement in skewed, non-coplanar junctions where axes do not intersect. Generating a hexahedral mesh for the current skew branch would require complex blocking and could result in cells with high non-orthogonality near the intersection. Polyhedral meshing, conversely, provides a high-quality conformal transition at the skew-junction interface, maintaining an orthogonal quality superior to that of tetrahedral meshes while requiring fewer cells to achieve the same level of accuracy.

The computational domain was discretized by unstructured polyhedral grid cells, as shown in Figure 3. Polyhedral cells were selected for their inherent ability to resolve complex flow structures and their enhanced numerical stability in capturing high-gradient regions with lower cell counts compared to tetrahedral meshes. To ensure the accurate resolution of the near-wall physics and the development of the boundary layer, five layers of boundary layer mesh were built to deal with the large amplitude of velocity gradient within boundary layers near the wall. This layer consists of five orthogonal prismatic cells with a stretching growth rate of 1.2. The total thickness of the prism layer was calibrated to ensure that the boundary layer was sufficiently contained, facilitating an accurate transition from the wall-modeled to the wall-resolved regions. The refinement is critical for capturing the large amplitude of velocity gradients within the viscous sublayer.

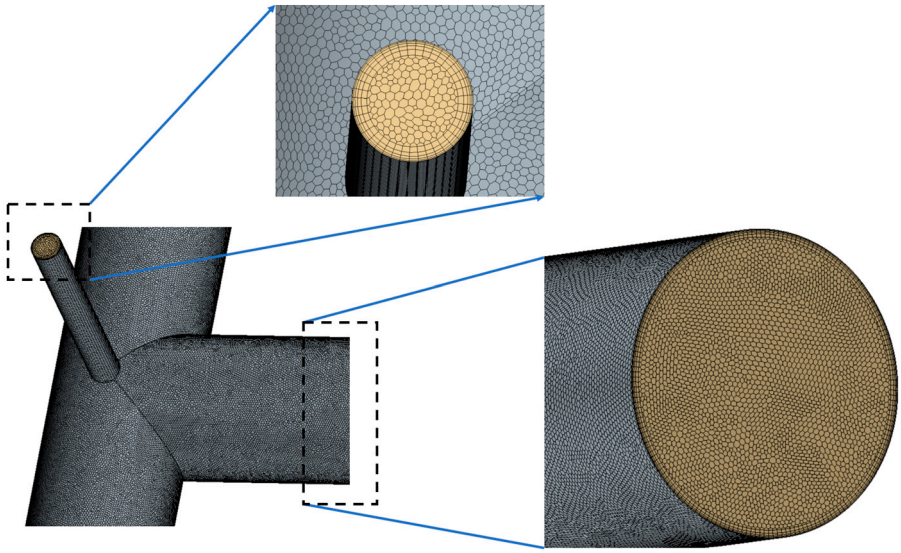


Figure 3. Grid generation for the pipe with a skew branch.

The boundary conditions consist of a mass flow inlet for both the main and branch pipes, and a pressure outlet boundary condition exerted on the upper and lower outlets. The no-slip wall boundary condition was imposed on the pipe wall.

4. Numerical Results

4.1. Operating Conditions

The numerical simulations were performed for the three geometric configurations detailed in Table 1, under a constant inflow rate of 650 m^3/h. The inflow rate of main inlet is 5000 m^3/h. As specified in Table 1, the primary variable across the three simulated cases is the geometric configuration of the branch inlet, while the total inflow rate was maintained at a constant value of 650 m^3/h. The main-pipe diameter ϕ_1 will be used as the reference length. Case 1 and Case 2 utilize an inclined branch with an inclusion angle (θ_0) of 45°, which is used as the reference angle. Case 2 introduces a spatial center offset (d) of 0.714 ϕ_1 to induce swirling flow. Case 3 serves as the orthogonal baseline with $\theta = 2\theta_0$ and $d = 0$.

Table 1. Case summary for internal flow simulations of the pipeline with a skew branch.

Case No.	Included Angle (θ/θ_0)	Offset (d/ϕ_1)	Inflow Rate (m^3/h)
1	1	0.0	650
2	1	0.714	650
3	2	0.0	650

The configurations provide two controlled comparisons. Case 3, with a 90° inclination and zero offset, is the orthogonal reference. Its comparison with Case 1, which has a 45° inclination and zero offset, examines the effect of inclination at zero offset. Case 2 retains the 45° inclination of Case 1 but introduces a 0.714 offset, allowing the effect of this installation change to be examined at a fixed angle.

4.2. Grid Convergence Studies

To ensure that the numerical results are independent of the spatial discretization, a systematic grid convergence study was performed using three unstructured polyhedral meshes. The mesh densities were categorized as Coarse (618,164 cells), Medium (1,151,464 cells), and Fine (2,513,568 cells). The refinement strategy involved increasing the

cell density globally while maintaining a consistent prism layer structure near the walls to ensure the accurate resolution of the boundary layer across all three levels.

As illustrated in Figure 4, several monitoring points were strategically arranged within the T-type pipeline system to evaluate the sensitivity of numerical results to mesh resolution. Probe 1 was located near the junction region to capture the local velocity variation induced by the interaction between the main flow and branch inflow, while Probe 2 was positioned at the central bottom region to monitor pressure fluctuations. Probe 3 was selected at the central location of the pipeline to evaluate the axial velocity evolution, and Probes 4 were placed at the centers of the upper and lower outlets to quantify the outlet flow-rate distribution. These monitoring locations were selected to characterize the representative hydrodynamic features, including velocity development, pressure redistribution, and flow imbalance caused by different branch configurations. The extracted variables from these probes were subsequently used for the grid convergence assessment to ensure that the numerical results were independent of spatial discretization.

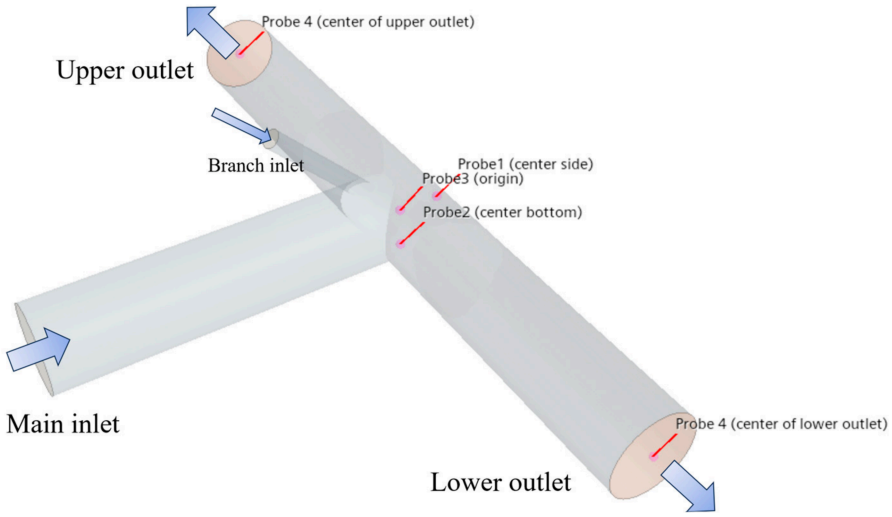


Figure 4. The probe points on the pipe flow.

The verification process focused on monitoring representative flow quantities across three progressively refined mesh densities, i.e., the static pressure at the central bottom (Probe 2), the axial velocity at the origin (Probe 3), and the mass flow rates at both outlets. As illustrated in the time-history plots in Figure 5, the velocity magnitude at the origin (Probe 3), the static pressure at the central bottom (Probe 2), and the mass flow rates at the upper and lower outlets were evaluated. For the velocity variation shown in Figure 5a, the results obtained using the coarse, medium, and fine meshes exhibit almost identical trends. Although slight discrepancies can be observed during the initial transient stage, the velocity values gradually converge as the simulation progresses. The difference between the medium and fine meshes becomes negligible after stabilization, indicating that further mesh refinement has limited influence on the predicted velocity field. The pressure evolution at the central bottom point is presented in Figure 5b. Similar to the velocity results, pressure fluctuations occur during the early stage due to the development of pressure redistribution within the T-junction region. With increasing simulation time, all mesh configurations show consistent pressure variation patterns. The close agreement between the medium and fine meshes confirms that the selected mesh resolution is sufficient to capture the pressure characteristics induced by the complex branch flow interaction.

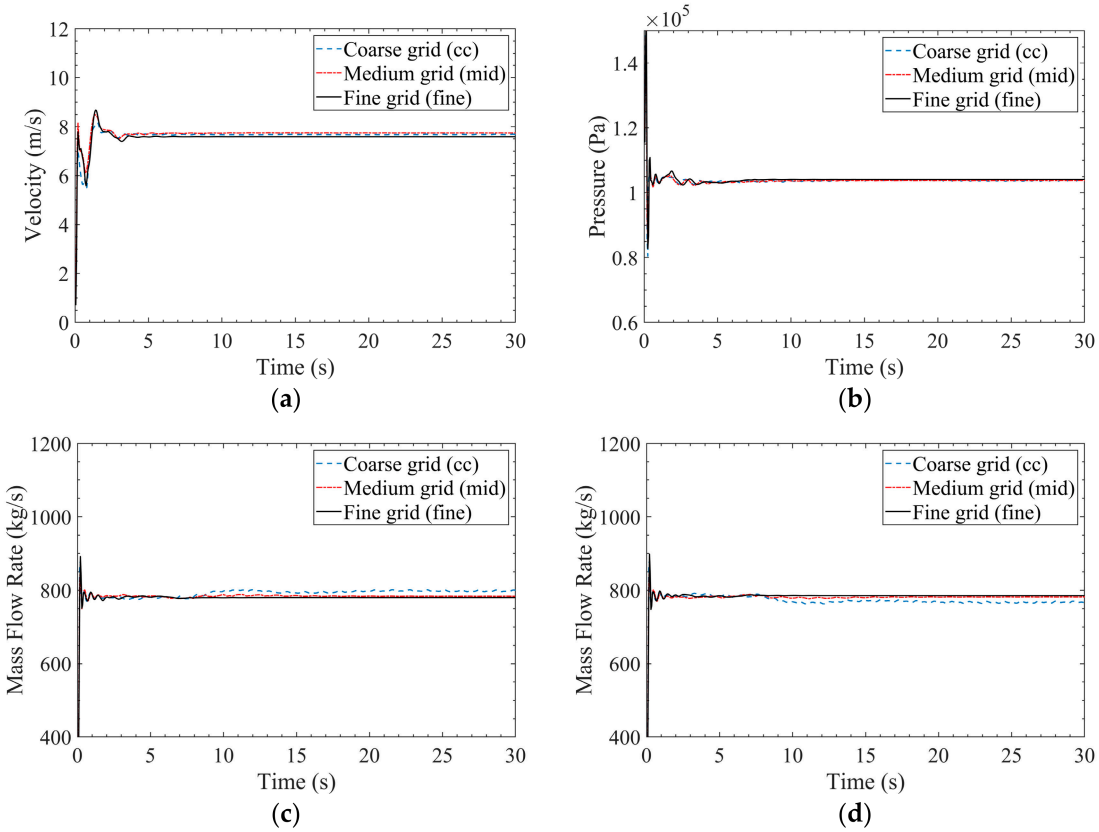


Figure 5. Grid convergence study for (**a**) the velocity at the central point (Origin point); (**b**) the pressure at the central bottom point; (**c**) the mass flow rate at the upper outlet; (**d**) the mass flow rate at the lower outlet.

The outlet mass flow rates are compared in Figure 5c,d. Since accurate prediction of outlet flow distribution is the primary objective of this study, these parameters provide a direct evaluation of the mesh influence on flow-control performance. The upper and lower outlet flow rates gradually stabilize with time, and the predictions from the medium and fine meshes show nearly identical results. The coarse mesh produces slightly larger deviations, particularly during the transient stage, due to insufficient resolution of the strong velocity gradients and secondary flow structures near the branch junction.

Quantitatively, the deviation in velocity and mass flow rate between the Medium and Fine grids was found to be less than 0.3%, indicating that further refinement would not significantly alter the flow characteristics. Based on this convergence analysis, the Fine mesh was selected for all subsequent internal flow simulations. This choice provides sufficient resolution to capture the complex swirling vortices and high-gradient pressure fields induced by the skew branch pipe with high fidelity, while maintaining computational efficiency. This resolution was thus adopted for all subsequent analyses to ensure the high-fidelity capture and resolution of the intricate turbulent swirling structures inherent to the flow field.

4.3. Velocity Fields and Flow Rates

The effects of the branch inclination angle and center offset on the internal hydrodynamic characteristics were evaluated by comparing the time histories of representative monitoring variables and the spatial distributions of velocity magnitude. Because the inlet flow rates and the remaining numerical settings were maintained consistently among the three cases, the differences observed in this section can be attributed primarily to the geometric configuration of the branch pipe. All three cases exhibited an initial transient

stage, followed by a gradual attenuation of the oscillations. Unless otherwise stated, the following discussion refers to the quasi-steady results obtained.

4.3.1. Velocity Fields and Swirling Flow Mechanism

Figure 6 presents the time histories of the velocity magnitude at Probe 3, which is located at the origin of the T-junction. Pronounced oscillations occurred during the first several seconds because the branch jet, main-pipe flow, and pressure field were still undergoing mutual adjustment. The oscillations subsequently decayed, and the velocities approached stable values of approximately 7.8 m/s, 4.9 m/s, and 7.6 m/s for Cases 1, 2 and 3, respectively.

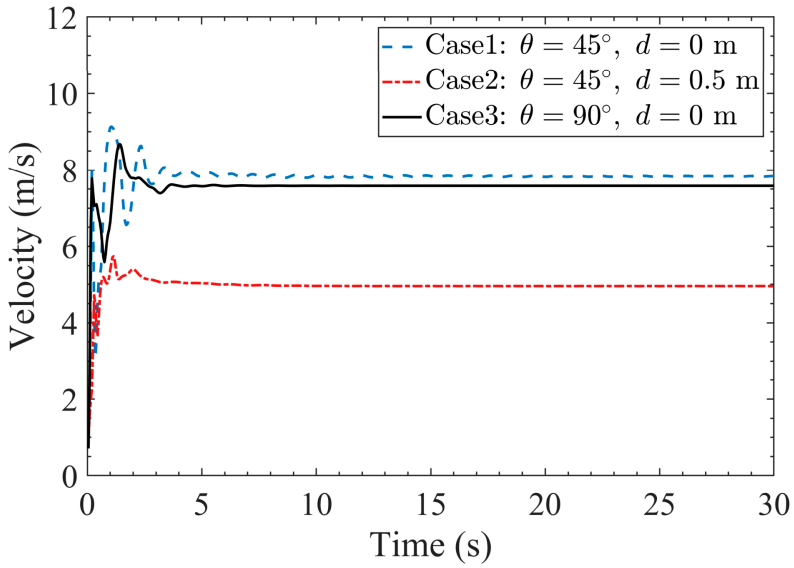


Figure 6. Time histories of the velocity at the central point (Origin point) for different geometries.

A comparison between Cases 1 and 2 demonstrates that introducing a center offset of d = 0.5 m considerably decreases the local velocity at the origin, even though the branch angle and inlet flow rates remain unchanged. The steady velocity in Case 2 is approximately 35–40% lower than that in Case 1. This behavior results from the redistribution of axial momentum into the circumferential direction caused by eccentric branch injection. This reduction does not represent a corresponding decrease in the total pipeline discharge. Instead, the eccentric branch inlet displaces the high-velocity jet away from the geometric center of the main pipe and redirects part of its momentum into the tangential direction, thereby inducing a swirling motion via conservation of angular momentum. Consequently, the origin is no longer located within the principal high-speed flow core. The slightly lower velocity of Case 3 relative to Case 1 is associated with the different momentum-exchange mechanism produced by the normal branch injection.

The velocities measured at the central points of the upper and lower outlets are compared in Figure 7. For the upper outlet, the final velocities are approximately 1.0, 1.1, and 1.5 m/s for Cases 1, 2 and 3, respectively. At the lower outlet, the corresponding values are approximately 1.25 m/s, 1.2 m/s and 1.5 m/s. Thus, Case 1 exhibits a clear pointwise velocity difference between the two outlets. Introducing the center offset increases the velocity at the center of the upper outlet while slightly reducing that at the lower outlet, thereby decreasing the local velocity difference. Case 3 produces nearly identical center-point velocities at the two outlets under the present operating condition.

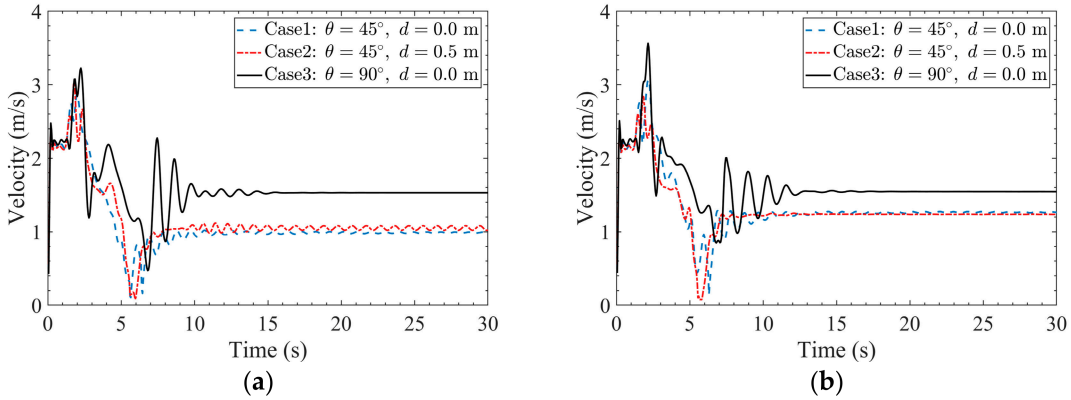


Figure 7. Time histories of the velocity at one point: (**a**) The velocity at the central point of the upper outlet; (**b**) The velocity at the central point of the lower outlet.

The transient response also depends on the branch geometry. Case 3 exhibits relatively large and long-lasting oscillations between approximately 5 s and 12 s, particularly at the outlet monitoring points. The normal branch jet directly impinges on the opposite region of the junction and generates a strong transient redistribution of momentum before the flow is divided between the two outlets. In comparison, the oscillations in Cases 1 and 2 decay more rapidly. Nevertheless, the center-point velocities should not be interpreted as area-averaged outlet velocities because the profiles are strongly non-uniform, especially in the presence of secondary and swirling flows. The area-integrated mass flow rates are therefore discussed separately in Section 4.3.2.

The velocity distributions at the inlet and outlet sections and streamlines in the pipe are shown in Figure 8. The relatively small diameter of the branch pipe produces a high-speed branch jet, whereas substantially lower velocities occur over most of the main-pipe and outlet cross-sections. For the inclined configurations, the high-speed region is circumferentially displaced as the branch flow enters the main stream. This displacement is more evident in Case 2 because the branch axis does not intersect the main-pipe axis. In contrast, the velocity pattern generated by the orthogonal branch in Case 3 is comparatively symmetric with respect to the branch-injection plane.

In all three configurations, the streamlines in the main inlet are approximately aligned with the pipe axis before undergoing substantial curvature within the junction and dividing toward the two outlets. It can be observed that the branch inlet introduces a localized high-velocity jet with the streamlines near the branch entrance and the junction. Farther downstream, winding streamlines extend into both outlet pipes, indicating that the flow retains a non-axial component rather than immediately becoming unidirectional. For the inclined configuration without an offset (Case 1, Figure 8a), the branch jet enters the junction obliquely and undergoes a sharp change in direction as it interacts with the main flow. Introducing an offset of d = 0.5 m (Case 2, Figure 8b), the high-velocity streamline bundle appears more elongated across the junction toward the lower-left outlet. The surrounding streamlines are correspondingly redirected, and the offset modifies the spatial development of the jet–main-flow interaction and the associated three-dimensional flow structure. For Case 3 in Figure 8c, the branch jet enters perpendicular to the main-inlet direction and forms a concentrated turning region beneath the branch opening. Distinct helically wound streamlines extend from the junction into both outlet pipes. The comparison shows that the branch inclination and offset affect the location of jet deflection, the arrangement of curved streamlines near the junction, and the downstream development of secondary motion.

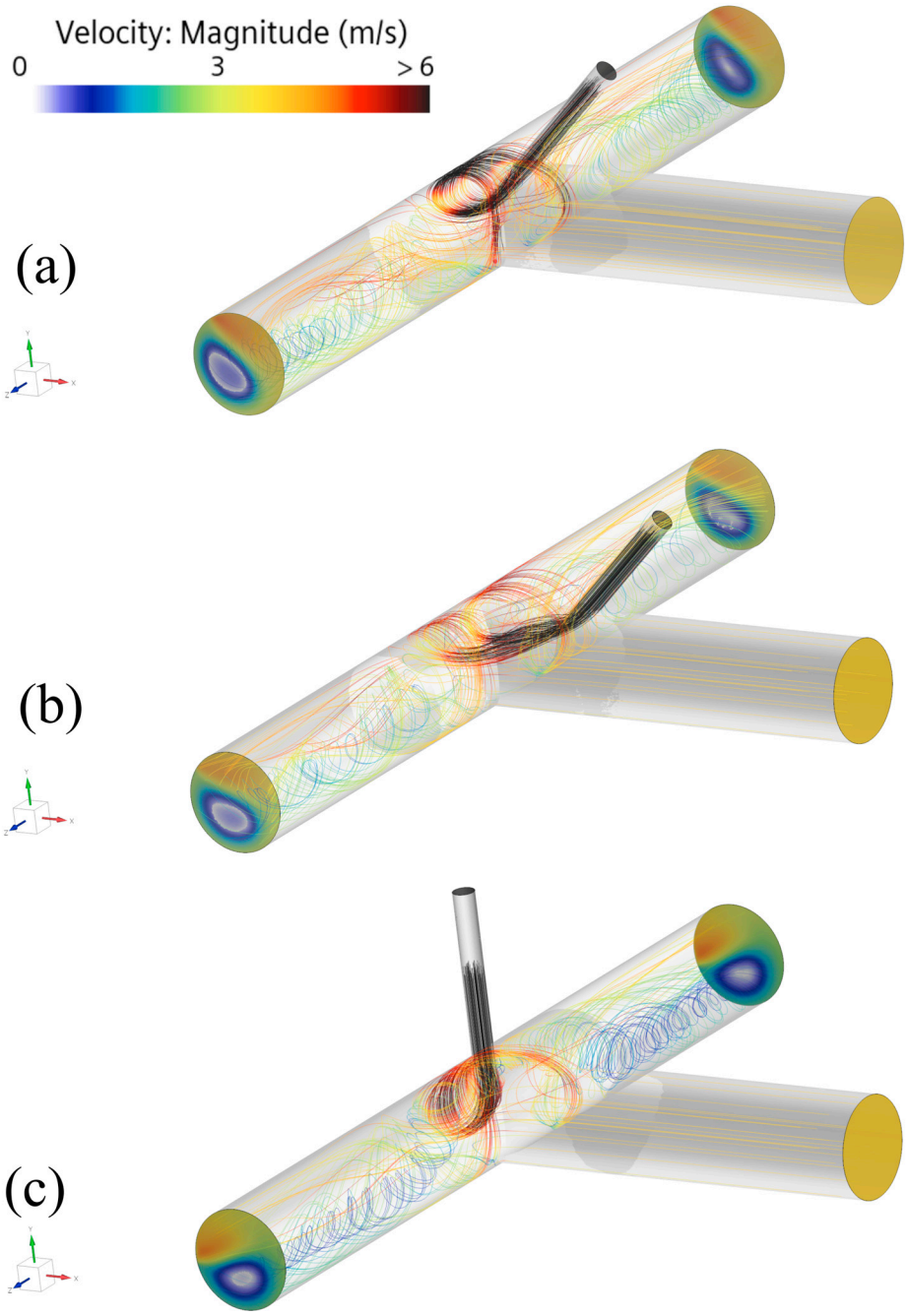


Figure 8. Velocity contour at the inlet and outlet and streamlines in the pipe: (**a**) $\theta = 45°$ and $d = 0.0$ m; (**b**) $\theta = 45°$ and $d = 0.5$ m; (**c**) $\theta = 90°$ and $d = 0.0$ m.

Further details of the internal velocity structures are provided by the contours on the $x = 0$, $y = 0$, and $z = 0$ planes in Figures 9–11. On the $x = 0$ plane, as shown in Figure 9, Cases 1 and 2 display an asymmetric combination of high- and low-velocity regions around the junction. The inclined branch jet creates a high-speed core near the central region, while low-velocity zones develop adjacent to the pipe walls as a result of flow turning and local separation. With the introduction of the center offset in Case 2, the high-speed core shifts away from the geometric center, and the low-velocity region becomes spatially redistributed. By comparison, Case 3 presents a more symmetric velocity pattern, with the normal branch jet generating a central high-speed region and paired low-speed zones on the two sides.

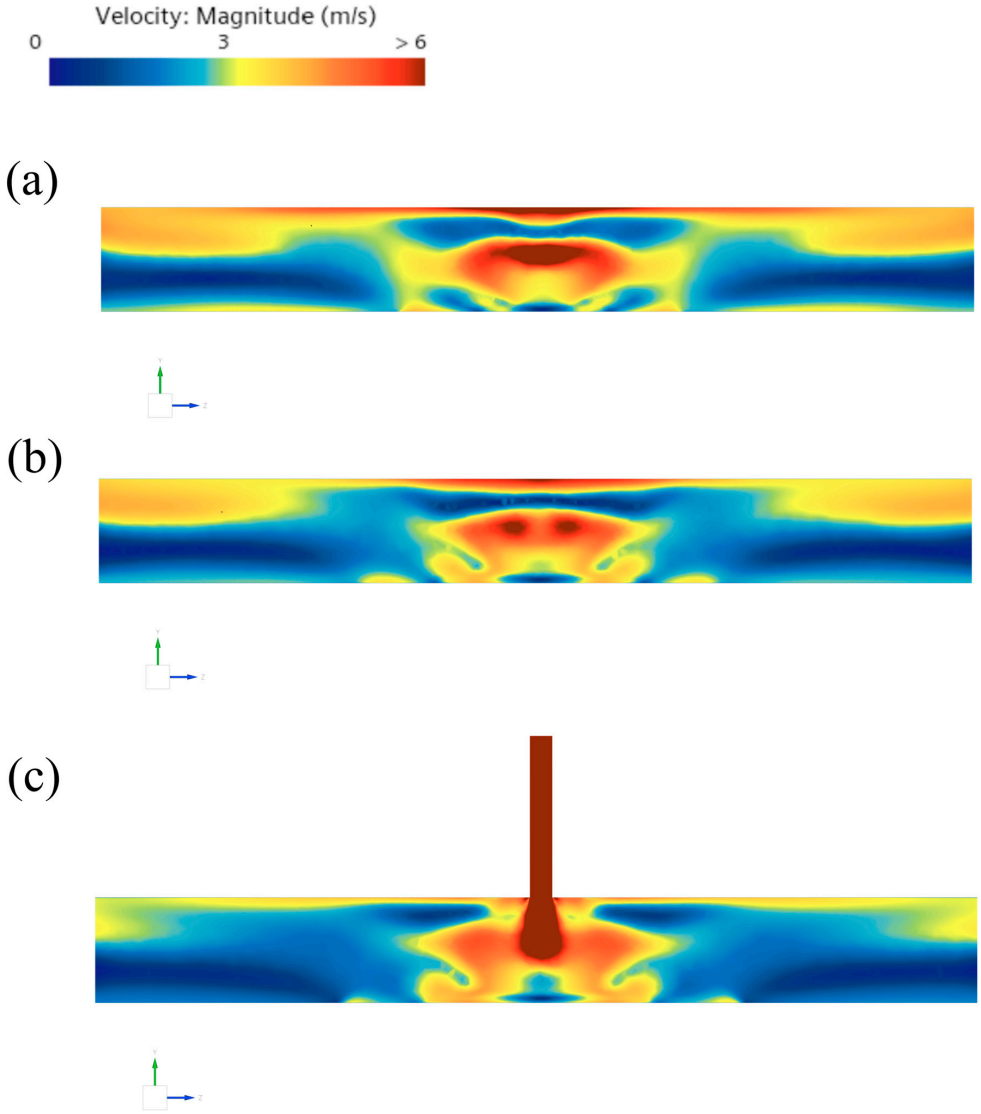


Figure 9. Velocity contour at the plane x = 0 m: (**a**) θ = 45° and d = 0.0 m; (**b**) θ = 45° and d = 0.5 m; (**c**) θ = 90° and d = 0.0 m.

The contours on the y = 0 plane in Figure 10 show that the flow accelerates through the central junction before entering the two outlet sections. Extended low-velocity layers appear near the outlet walls, while the faster-moving fluid is concentrated closer to the central portion of the junction. Cases 1 and 2 display different positions and shapes of the high-speed region despite having the same branch angle. This confirms that the center offset modifies not only the local velocity magnitude but also the downstream momentum distribution. Case 3 again exhibits a more symmetric distribution because the branch inflow is introduced without eccentricity.

The z = 0 plane contours in Figure 11 provide the clearest illustration of the effect of branch eccentricity. In Case 1, the centered inclined jet passes through the junction and produces a high-velocity region close to the origin. A low-velocity recirculation or separation region forms near the curved wall opposite the incoming main flow. In Case 2, the branch jet enters the main pipe tangentially and the high-speed region is displaced toward one side of the pipe. The low-speed zone is correspondingly shifted and elongated, indicating a strong three-dimensional redistribution of the flow. The combined observations from the three orthogonal planes indicate that the center offset rotates the high-speed flow core around the pipe cross-section, which is consistent with the generation of an eccentric

swirling motion. In Case 3, the normal jet produces a more symmetric impact-and-turning pattern and a concentrated low-velocity zone near the rounded wall.

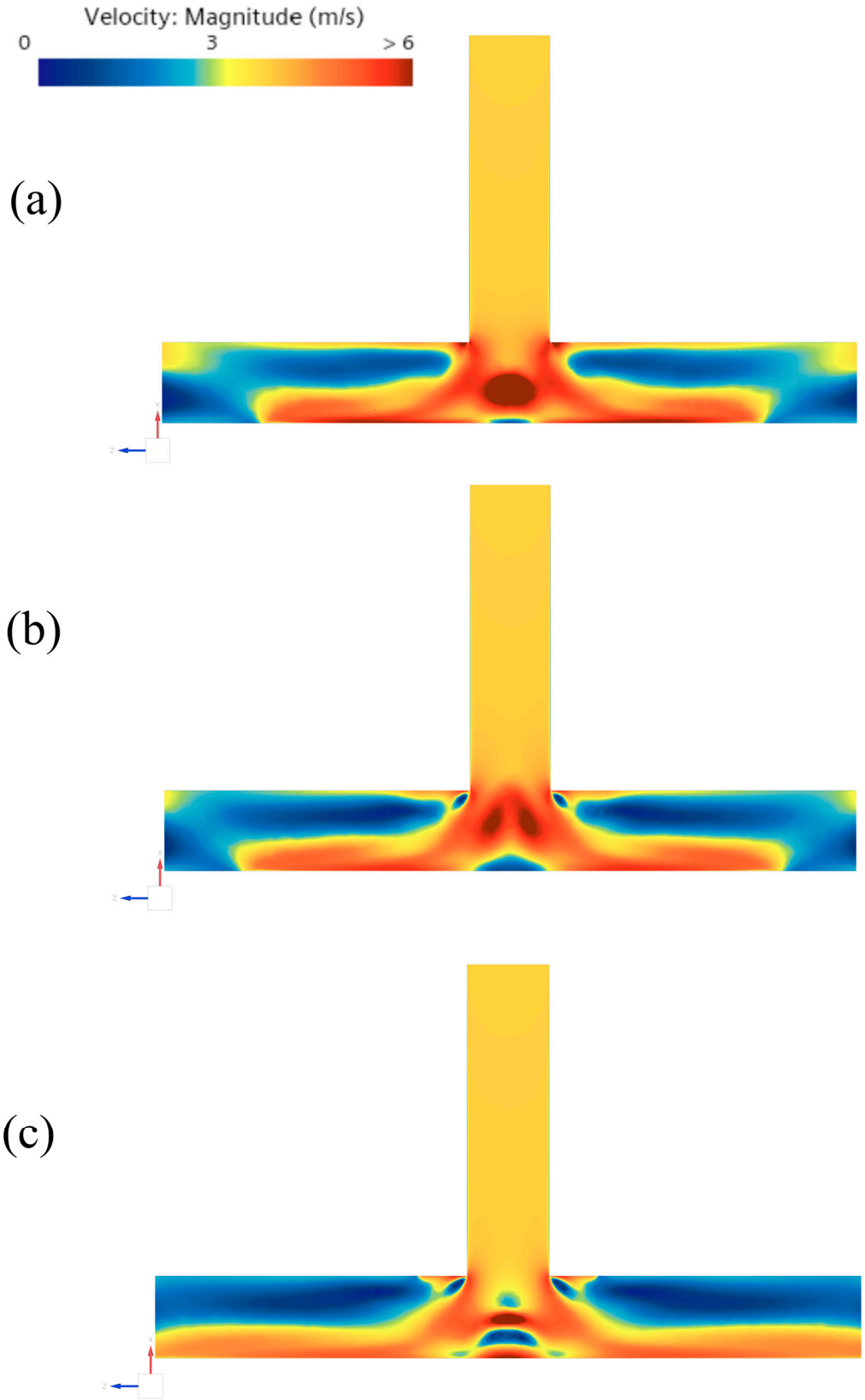


Figure 10. Velocity contour at the plane y = 0 m: (**a**) θ = 45° and d = 0.0 m; (**b**) θ = 45° and d = 0.5 m; (**c**) θ = 90° and d = 0.0 m.

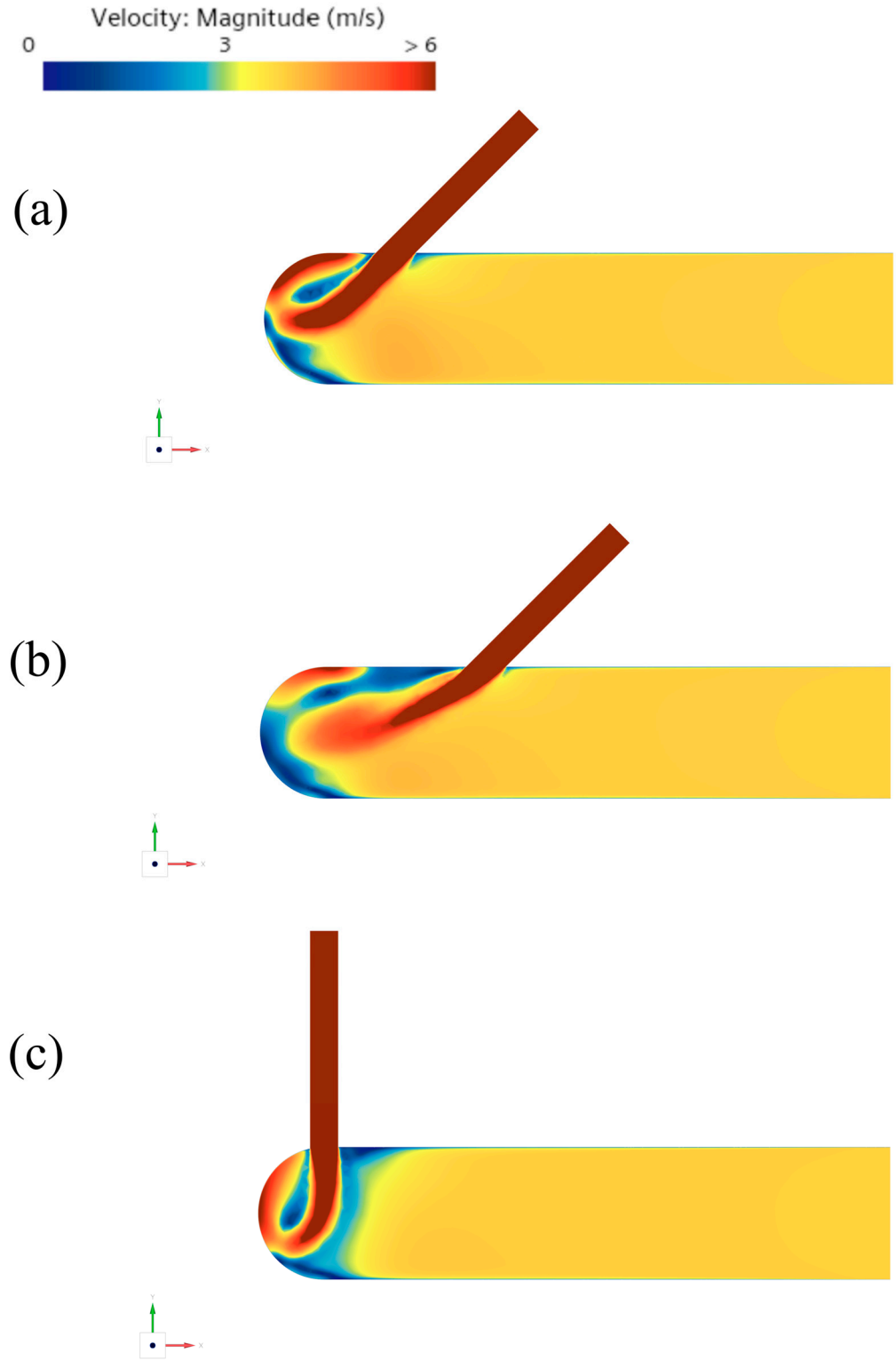


Figure 11. Velocity contour at the plane z = 0 m: (**a**) θ = 45° and d = 0.0 m; (**b**) θ = 45° and d = 0.5 m; (**c**) θ = 90° and d = 0.0 m.

The different flow patterns observed among the three cases can be explained by the variation in momentum exchange. In the conventional coplanar branch configuration (Case 1), the branch flow enters the main pipeline with its momentum primarily aligned with the axial direction of the main pipe. Although the inclined branch modifies the local velocity distribution, the injected momentum is mainly converted into axial momentum after the flow impinges with the main stream. Consequently, the generated secondary flow

remains relatively weak, and the high-speed region remains concentrated near the central plane of the junction. In contrast, the introduction of the spatial center offset in Case 2 changes the interaction mode between the branch jet and the main flow. Because the branch axis is shifted away from the centerline of the main pipe, the incoming branch flow no longer impinges symmetrically on the main stream. Instead, the offset geometry introduces an additional circumferential momentum component. The branch jet therefore possesses both axial and tangential momentum components when entering the main pipeline, resulting in a three-dimensional swirling motion downstream of the junction.

Overall, the velocity results indicate that the center offset functions as a momentum redistribution parameter rather than merely a geometric displacement. By introducing a circumferential momentum component, the skew branch modifies the three-dimensional velocity structure, induces swirling motion, and provides a passive mechanism for regulating downstream flow distribution.

4.3.2. Flow Rates

Figure 12 compares the time histories of the mass flow rates at the upper and lower outlet planes. All curves show a short initial oscillatory period, after which the outlet mass flow rates become nearly constant. The transient fluctuations are substantially attenuated after approximately 5–10 s, indicating that the global flow division reaches a stable condition earlier than some of the local velocity and pressure variables:

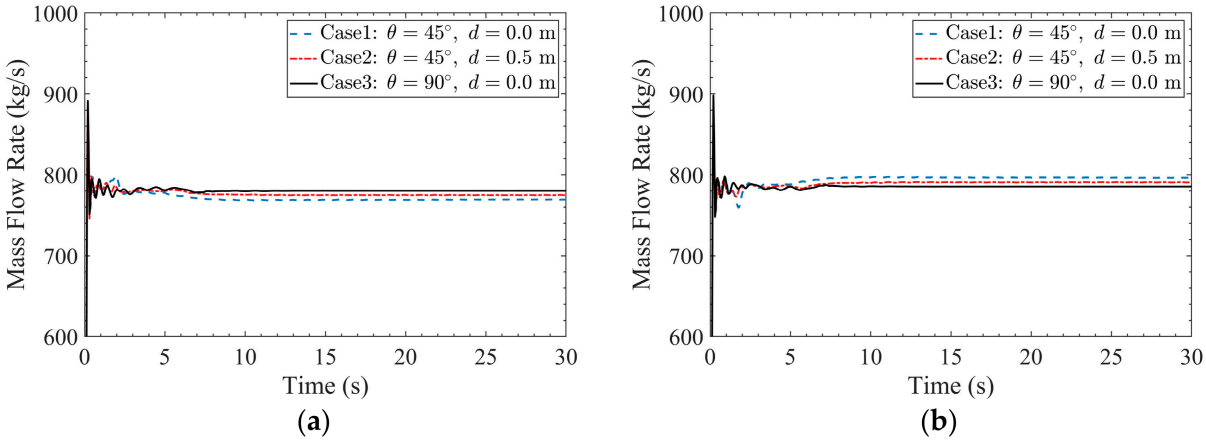


Figure 12. Time histories of the mass flow rate at the outlet plane: (**a**) The mass flow rate at the upper outlet; (**b**) The mass flow rate at the lower outlet.

At the upper outlet, the steady mass flow rates increase in the order of Case 1, Case 2, and Case 3. The values are 770, 775 and 780 kg/s, respectively. The opposite ordering is observed at the lower outlet, where the steady mass flow rates are approximately 800, 790, and 785 kg/s for Cases 1, 2, and 3, respectively. The sum of the two outlet mass flow rates remains almost unchanged among the three configurations, confirming that the branch geometry primarily redistributes the incoming flow between the outlets rather than altering the total pipeline throughput.

Case 1 produces the largest outlet imbalance, with the lower-outlet mass flow rate exceeding that of the upper outlet by approximately 20~30 kg/s. When the center offset is introduced in Case 2, part of the flow is transferred from the lower outlet to the upper outlet. The resulting mass-flow difference is reduced to approximately 10–15 kg/s, representing a substantial improvement relative to the centered branch configuration. This variation is consistent with the displacement of the high-speed core and the modified pressure field generated by the tangential branch inflow.

Among the three configurations investigated, Case 3 provides the closest outlet mass flow rates under the prescribed operating condition, with a remaining difference of only several kilograms per second. Nevertheless, the comparison between Cases 1 and 2 clearly shows that the center offset can be used to continuously tune the flow division while retaining the same branch angle and pump operating condition. Although exact equality is not obtained for the single tested offset of d = 0.5 m, the systematic shift in the two outlet flow rates indicates that an equilibrium condition could potentially be identified through further optimization or interpolation of the offset distance. Therefore, the center offset can be regarded as a practical passive-control parameter for regulating water delivery to different aquaculture tanks.

4.4. Pressure Fields

The influence of the branch geometry on the pressure response was first evaluated using the time histories at the outlet planes and at the monitoring points near the junction. Figure 13 shows that the upper-outlet pressures of all three cases gradually converged. Although transient oscillations occur during the initial 10–15 s, the final differences among the three configurations are very small. This indicates that the pressure recovery at the upper outlet is only weakly affected by the branch geometry after the flow has reached a stable state. A greater geometry-dependent difference is observed at the lower outlet. Case 2 therefore produces the lowest pressure at the lower-outlet monitoring position. This result is consistent with the strong redistribution of momentum caused by the eccentric branch jet. Case 3 exhibits the largest pressure oscillations during the early transient stage, but these oscillations decay and the pressure eventually becomes stable.

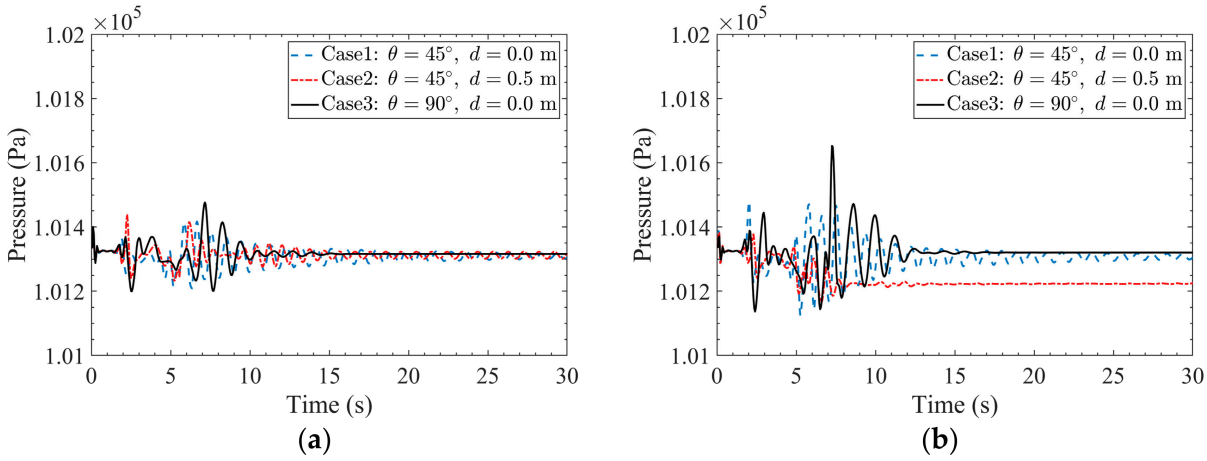


Figure 13. Time histories of the pressure at the outlet plane: (**a**) The pressure at the upper outlet; (**b**) The pressure at the lower outlet.

The internal pressure histories in Figure 14 show much greater differences than those recorded near the outlet planes. The centered 45° branch therefore produces the highest local pressure at this position. Introducing the offset reduces the pressure by shifting the high-momentum jet and its associated stagnation region away from the center-bottom monitoring point. The considerably lower value in Case 3 indicates that the principal impingement and high-pressure region generated by the orthogonal branch is located elsewhere in the junction.

At the center-side point (−0.35, 0, 0), the pressure differences are smaller. The contrast between the two monitoring positions shows that branch geometry primarily modifies localized pressure loading near the jet impingement and turning regions, while its influence

becomes weaker farther away from the principal interaction zone. It also shows that similar outlet pressures do not necessarily imply similar internal wall-pressure distributions.

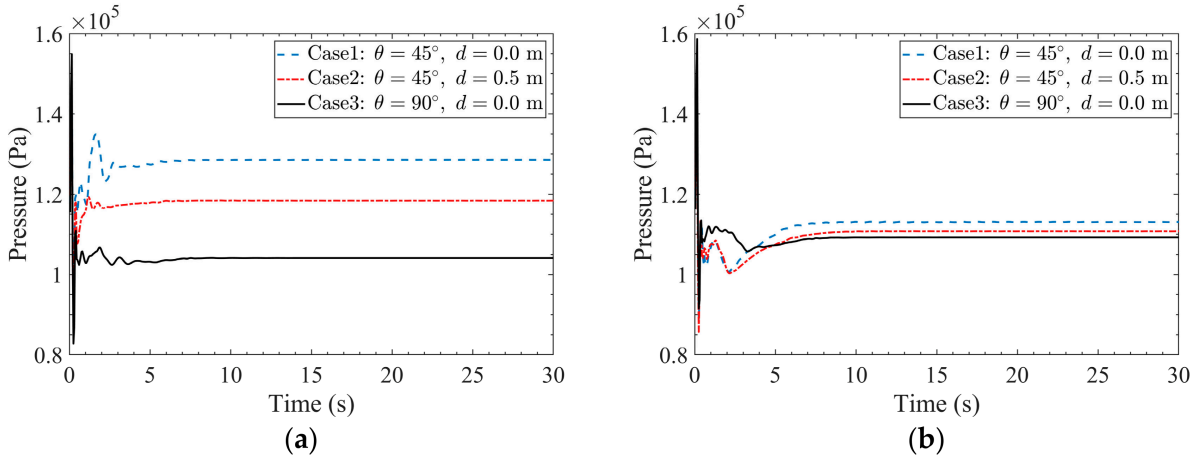


Figure 14. Time histories of the pressure at the central plane: (**a**) The pressure at the center bottom point (0, −0.35, 0); (**b**) The pressure at the center side point (−0.35, 0, 0).

Figure 15 presents the pressure contours on the structural surfaces using a common pressure scale. In all cases, relatively high pressures occur along the upstream main pipe and branch inlet, whereas low-pressure bands develop around the T-junction as the flow accelerates, separates, and turns toward the two outlets. For Case 1, a broad pressure gradient surrounds the intersection, with alternating high- and low-pressure regions extending circumferentially along the outlet pipe. This pattern reflects the direct interaction between the centered inclined jet and the main flow. The pressure footprint changes markedly when the offset is introduced. In Case 2, the high-pressure region near the branch entrance is displaced toward one side of the main pipe, and a localized low-pressure zone develops near the skewed junction. Compared with Case 1, the pressure field is more circumferentially asymmetric, which is consistent with the tangential injection and swirling flow identified from the velocity contours. Case 3 produces a comparatively symmetric distribution, with a concentrated high-pressure stagnation region close to the normal branch entrance and paired low-pressure bands on the surrounding outlet surfaces.

The pressure contours on the x = 0 plane are compared in Figure 16. Cases 1 and 2 display a high-pressure region on one side of the junction and an extended low-pressure region on the opposite side. The center offset changes both the size and position of these regions, with the low-pressure core becoming more compact and spatially shifted in Case 2. The vertically asymmetric pressure pair is a consequence of the skewed momentum input. In Case 3, two relatively symmetric low-pressure lobes form on either side of the branch, while a high-pressure region is concentrated near the central impingement zone.

Figure 17 shows the pressure distributions on the y = 0 plane. For the two configurations, high pressure develops beneath the branch-junction region, whereas elongated low-pressure zones extend into the adjacent outlet sections. The pressure magnitude and spatial extent are greater in Case 1, which is consistent with the higher pressure recorded at the center-bottom probe. The offset in Case 2 weakens and redistributes this high-pressure footprint. In Case 3, a compact low-pressure pocket is located immediately below the normal branch jet and is surrounded by relatively high-pressure fluid. This localized pattern reflects the direct impingement, flow separation, and subsequent division of the branch flow.

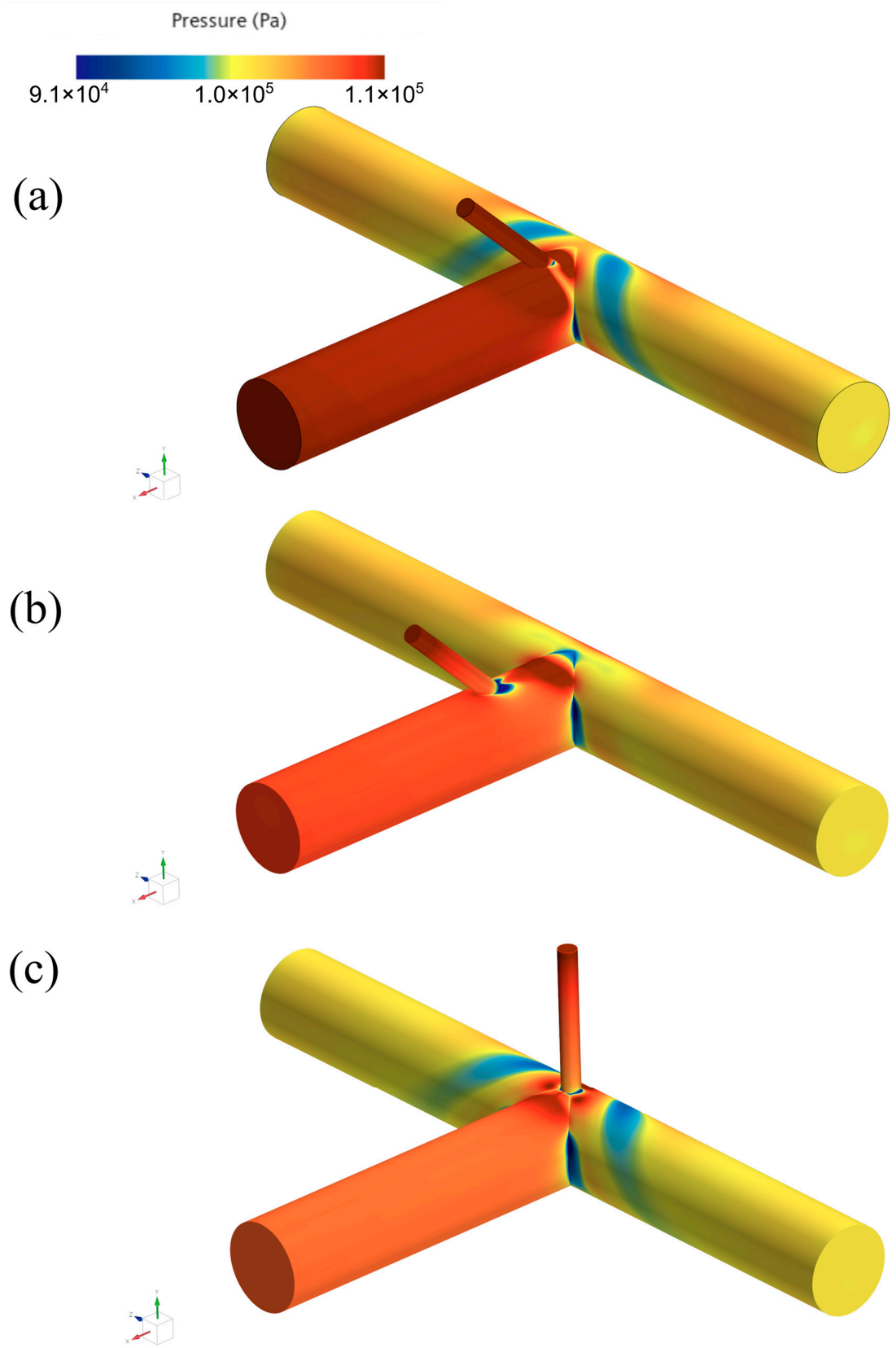


Figure 15. Pressure contour on the structural surface: (**a**) θ = 45° and d = 0.0 m; (**b**) θ = 45° and d = 0.5 m; (**c**) θ = 90° and d = 0.0 m.

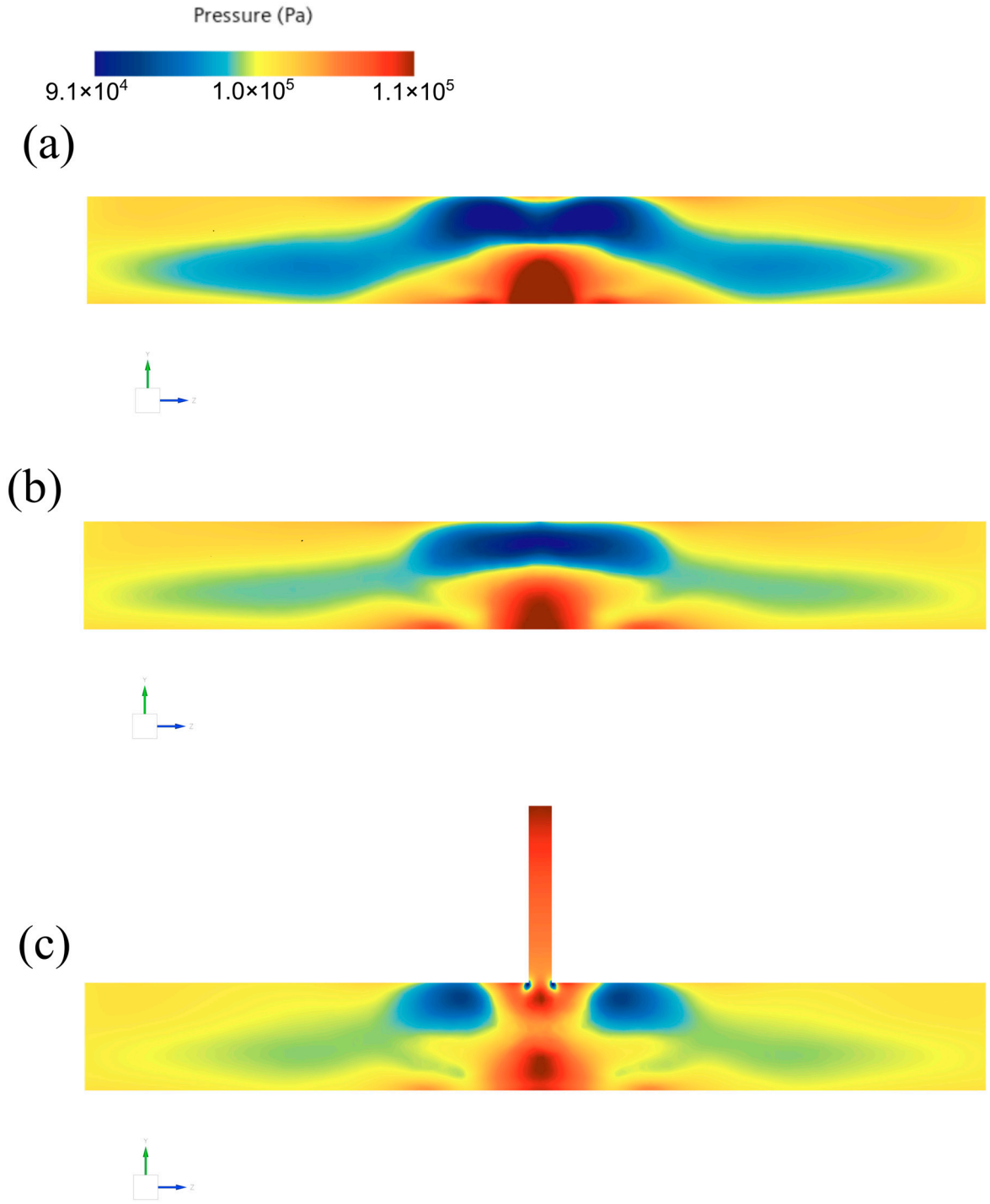


Figure 16. Pressure contour at the plane x = 0 m: (**a**) θ = 45° and d = 0.0 m; (**b**) θ = 45° and d = 0.5 m; (**c**) θ = 90° and d = 0.0 m.

The z = 0 contours in Figure 18 further show the influence of the skew branch geometry. A distinct low-pressure region occurs near the rounded wall of the main pipe in all three cases, corresponding to the strong curvature and local separation of the flow. In Case 1, this region remains relatively close to the geometric centerline, while the surrounding pipe section is dominated by high pressure. In Case 2, the principal low-pressure region is displaced toward one side, and an additional localized pressure depression appears near the branch throat. These features confirm that the offset branch produces a fully three-dimensional

and asymmetric pressure field. The pressure pattern of Case 3 is more nearly aligned with the branch-injection plane and remains comparatively symmetric downstream.

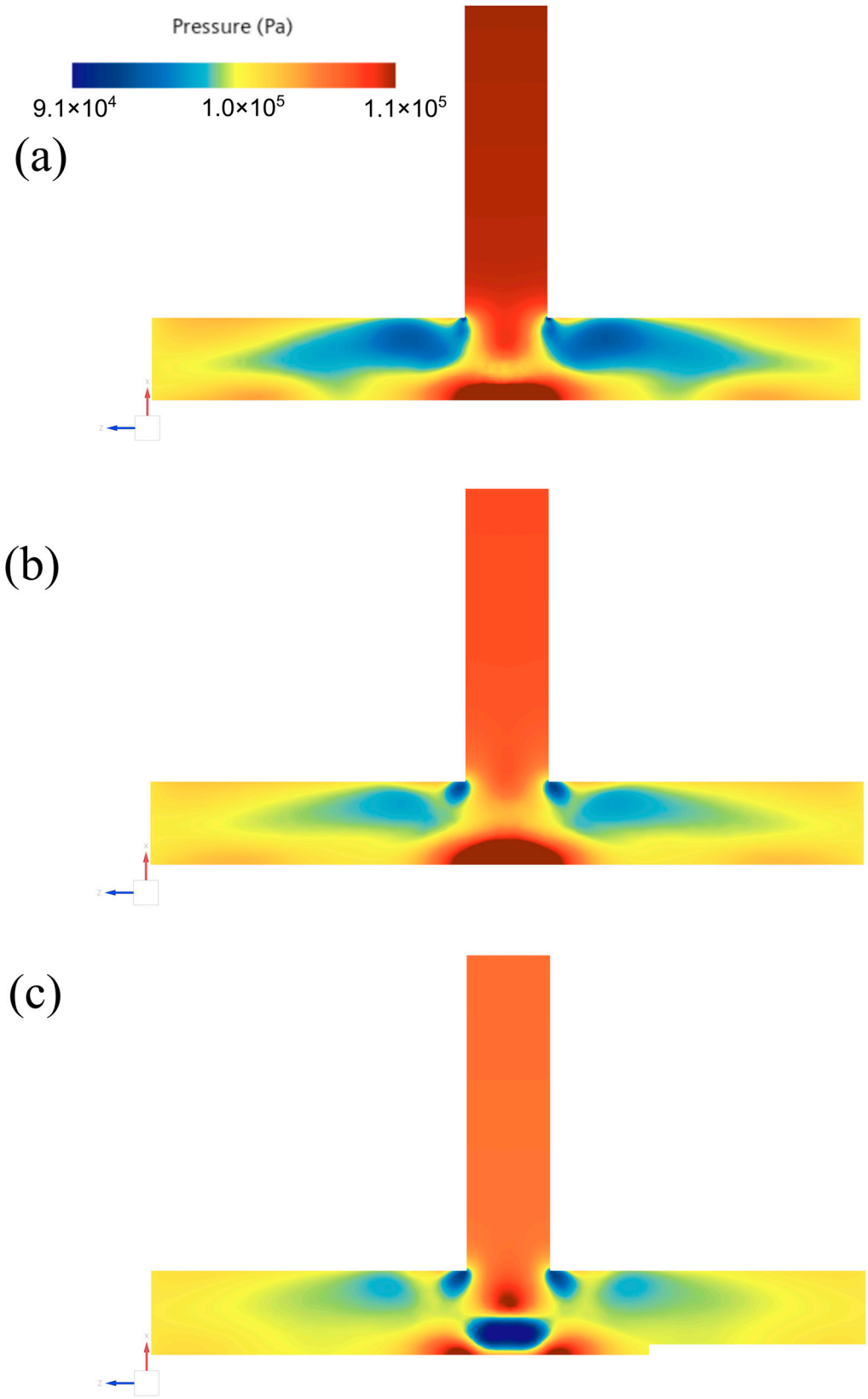


Figure 17. Pressure contour at the plane y = 0 m: (**a**) θ = 45° and d = 0.0 m; (**b**) θ = 45° and d = 0.5 m; (**c**) θ = 90° and d = 0.0 m.

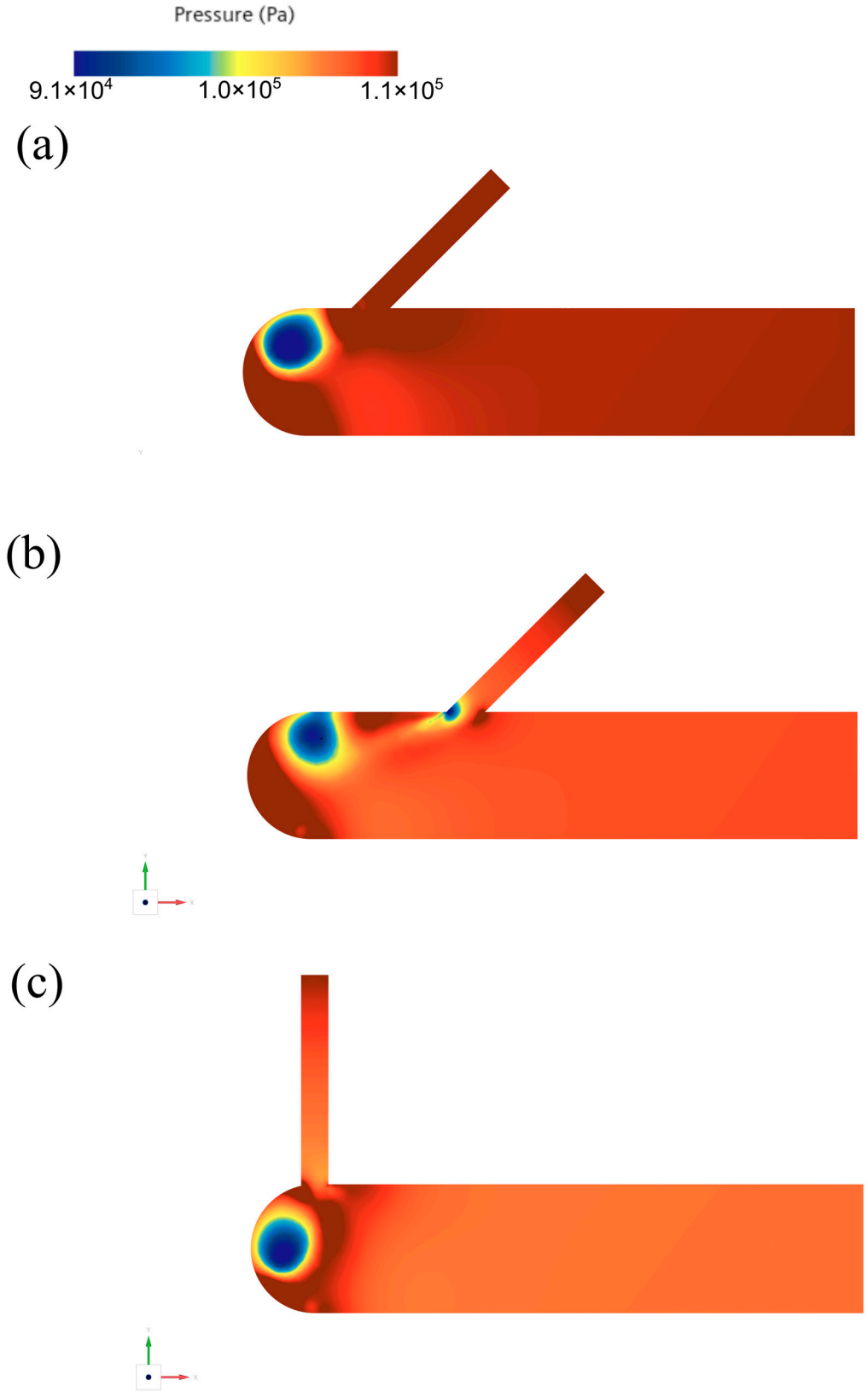


Figure 18. Pressure contour at the plane z = 0 m: (**a**) θ = 45° and d = 0.0 m; (**b**) θ = 45° and d = 0.5 m; (**c**) θ = 90° and d = 0.0 m.

The pressure results indicate that the center offset can reduce the pressure at selected high-load regions and modify the pressure gradient responsible for the outlet flow division. However, the same offset also introduces stronger circumferential pressure asymmetry.

Therefore, optimization of a skew branch pipe should consider both hydraulic performance and structural loading. A configuration that improves outlet flow balance may still generate localized pressure gradients that contribute to flow-induced vibration and noise. The branch angle and center offset should consequently be optimized simultaneously to achieve an acceptable compromise among flow-rate uniformity, pressure loading, and operational stability.

4.5. Unsteady Flow with Time-Varying Inflows

An assessment based primarily on quasi-steady flow conditions does not fully characterize the response of the pipeline to time-varying inflows. In this section, to address this concern, we have added an unsteady operating condition with sinusoidally varying flow rates at both the main inlet and the branch inlet. The prescribed inlet conditions of both main pipe and branch are expressed as:

$$Q(t) = Q_0[1 + 0.5\sin(2\pi t/T)] \quad (11)$$

$$Q_1(t) = Q_{1,0}[1 + 0.5\sin(2\pi t/T)] \quad (12)$$

where Q_0 is the cycle-averaged flow rate and Q(t) is the instantaneous flow rate for the main inlet. $Q_{1,0}$ is the cycle-averaged flow rate and Q_1(t) is the instantaneous flow rate for the branch pipe. For the preliminary study, the cycle period, T, is set as 5.0 s, corresponding to a frequency of 0.2 Hz. Both inlet flow rates remain nonnegative, so the imposed boundary conditions include periodic reductions but do not prescribe inlet flow reversal. The additional case is designed to examine the evolution of the internal flow and outlet discharge during repeated acceleration and deceleration of the inlet streams. More general disturbances, including phase differences, unequal relative amplitudes, and different forcing frequencies, remain relevant directions for future investigation.

Figure 19 compares the velocity histories at the origin for the configuration with $\theta = 45°$ and $d = 0.0$ m under constant and sinusoidally varying inlet conditions. With constant inlet flow rates, the initial velocity fluctuations progressively decay, and the monitored velocity approaches approximately 7.8 m/s. In contrast, the time-varying inlet conditions produce sustained oscillations throughout the simulation. The recurring velocity maxima are about 50% higher than the constant-inlet reference value. The interval between successive peaks is approximately 5 s, consistent with the imposed inlet oscillation period. The nearly repeatable oscillations in the later cycles show that the junction-center velocity approaches a periodic state rather than a time-independent value. The time-varying inlet conditions also produce pronounced velocity fluctuations at the centers of both outlets, as shown in Figure 20. Under periodic forcing, the upper-outlet velocity exhibits recurring peaks of approximately 4.2 m/s in the later cycles, whereas the corresponding lower-outlet peaks reach approximately 5.4 m/s. These peak velocities are roughly four times their respective constant-inlet reference values. At both monitoring points, the velocity decreases to near-zero values during parts of each cycle. Thus, the two outlet locations exhibit different transient developments and different responses to the same inlet forcing. Compared with the relatively smooth oscillation at the junction center in Figure 19, the outlet signals in Figure 20 are more strongly distorted.

As shown in Figure 21, it illustrates the spatial variation in the pressure response to periodic inlet forcing. At the center-bottom point, the pressure under constant inlet conditions approaches approximately 1.3×10^5 Pa. The periodic maximum is approximately 25% higher than the constant-inlet reference pressure. This distinction indicates that both the initial pressure excursion and the subsequent cyclic variation should be considered when evaluating the pressure response at this location. At the center-side point, the constant-inlet

pressure approaches 1.13 × 10^5 Pa. However, the resulting peak-to-peak variation substantially smaller than that at the center-bottom point. The center-bottom pressure fluctuation is three times larger than the center-side fluctuation. In addition, the center-side pressure remains below its constant-inlet reference for a substantial portion of each cycle, showing that the periodic response is not simply symmetric about the corresponding steady value.

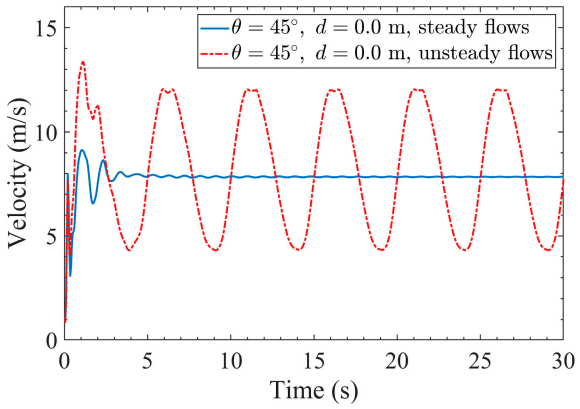


Figure 19. Time histories of the velocity at the central point (Origin point) for unsteady flows.

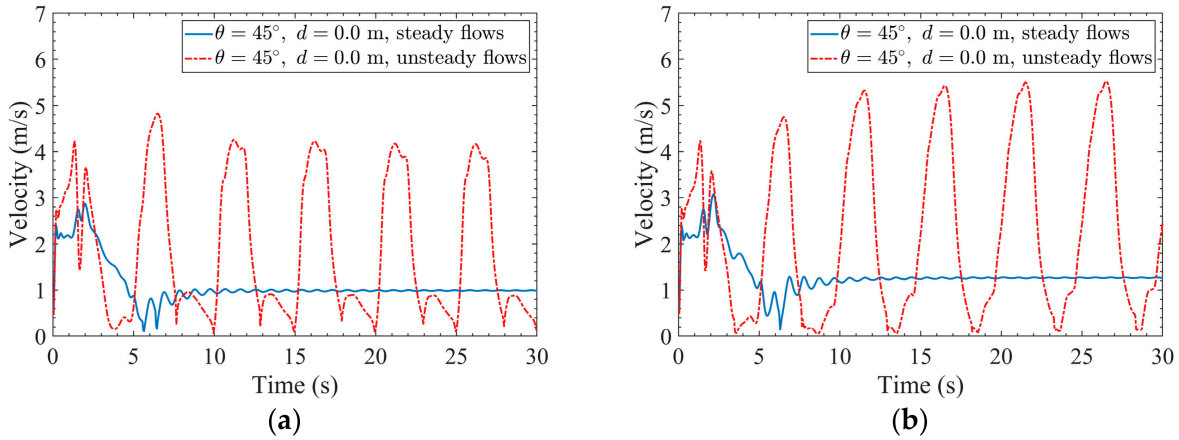


Figure 20. Time histories of the velocity at one point for unsteady flows: (**a**) The velocity at the central point of the upper outlet; (**b**) The velocity at the central point of the lower outlet.

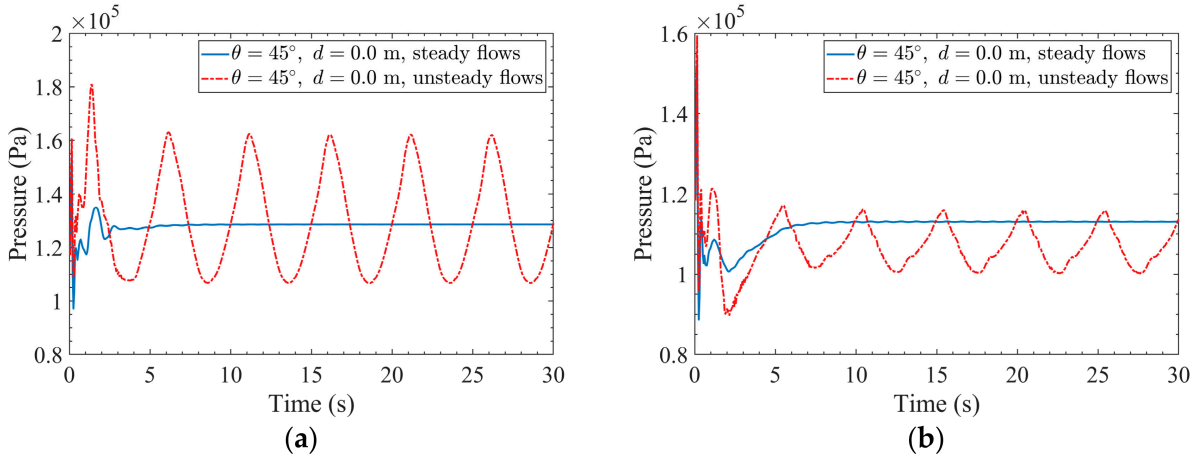


Figure 21. Time histories of the pressure at the central plane for unsteady flows: (**a**) The pressure at the center bottom point (0, −0.35, 0); (**b**) The pressure at the center side point (−0.35, 0, 0).

5. Conclusions

In this study, three-dimensional CFD simulations were performed to investigate the influence of a skew branch pipe on the internal flow characteristics and flow-rate distribution in a T-type pipeline system for an aquaculture vessel. Unlike conventional coplanar branch configurations, the proposed skew branch introduces an additional spatial degree of freedom through the center offset, enabling the modification of momentum transfer and secondary flow structures within the main pipeline. The main conclusions can be summarized as follows:

(1) The center offset of the skew branch pipe significantly modifies the internal velocity distribution. Compared with the conventional inclined branch without offset, introducing a spatial offset shifts the high-speed branch jet away from the geometric center of the main pipe and generates tangential momentum. The spatial offset introduces a moment arm relative to the main pipe axis, converting a portion of the linear momentum into angular momentum, thereby sustaining the swirling flow. As a result, the velocity core is redistributed within the junction region, and a three-dimensional swirling flow structure is formed downstream of the branch inlet. The velocity contours on different cross-sections showed that the offset parameter effectively controls the location and intensity of high- and low-velocity regions inside the pipeline.

(2) The skew branch provides an effective passive strategy for regulating outlet flow distribution. The outlet mass flow rates were strongly affected by the branch configuration. Although the total flow rate remained nearly unchanged among different cases, the distribution between the upper and lower outlets varied due to differences in momentum redistribution. Compared with the centered inclined branch, the offset configuration reduced the imbalance between outlet flow rates by transferring part of the flow momentum toward the upper outlet. These results indicate that the center offset shows potential as a geometric parameter for regulating flow distributions without modifying pump operating conditions.

(3) The branch geometry produces significant variations in local pressure fields. The introduction of a skew branch modifies the pressure distribution around the junction region by changing the location of flow impingement, separation and vortex development. The offset configuration reduced the local high-pressure concentration observed in the centered branch case while producing a more asymmetric circumferential pressure distribution. Although such pressure redistribution contributes to improved flow balancing, excessive asymmetry may increase local hydraulic loading and overall energy dissipation.

(4) The proposed skew branch configuration offers an alternative strategy for hydraulic optimization of large-scale aquaculture vessel pipeline systems. By utilizing geometric modification rather than additional active control components, the proposed method offers an additional geometric option for improving flow uniformity in multi-tank aquaculture vessels. However, the optimal design of skew branch pipes requires further investigation considering multiple parameters, including branch angle, center offset, operating flow conditions, and structural response. Future studies should integrate hydrodynamic optimization with flow-induced vibration and noise analyses to support the development of reliable and intelligent offshore aquaculture systems.

(5) The time-varying inlet conditions introduce additional local velocity and pressure excursions that must be considered alongside the quasi-steady results when assessing pipeline hydraulic performance.

Author Contributions: Conceptualization, W.H. and R.Z.; methodology, R.Z.; software, S.Y.; validation, W.H., S.Y. and R.Z.; formal analysis, W.H.; investigation, W.H., S.Y. and W.W.; resources, L.W.; data curation, L.W.; writing—original draft preparation, W.H., S.Y., W.W., L.W. and R.Z.; writing—review and editing, R.Z.; visualization, W.H.; supervision, R.Z.; project administration, R.Z.;

funding acquisition, W.H. and R.Z. All authors have read and agreed to the published version of the manuscript.

Funding: This work was financially supported by the National Key Research and Development Program of China (Grant No. 2022YFD2401101).

Institutional Review Board Statement: Not applicable.

Data Availability Statement: The original contributions presented in this study are included in the article. Further inquiries can be directed to the corresponding author.

Conflicts of Interest: The authors declare no conflicts of interest. Weitang Wang is employed by China State Shipbuilding Corporation Qingdao Beihai Shipbuilding Co., Ltd. The other authors declare no conflicts of interest. The company had no role in the design of the study; in the collection, analyses, or interpretation of data; in the writing of the manuscript, or in the decision to publish the results.

References

1. FAO. *The State of World Fisheries and Aquaculture 2024: Blue Transformation in Action*; Food and Agriculture Organization of the United Nations: Rome, Italy, 2024. [CrossRef]
2. Naylor, R.L.; Hardy, R.W.; Buschmann, A.H.; Bush, S.R.; Cao, L.; Klinger, D.H.; Little, D.C.; Lubchenco, J.; Shumway, S.E.; Troell, M. A 20-year retrospective review of global aquaculture. *Nature* **2021**, *591*, 551–563. [CrossRef]
3. Hvas, M.; Folkedal, O.; Oppedal, F. Fish welfare in offshore salmon aquaculture. *Rev. Aquac.* **2021**, *13*, 836–852. [CrossRef]
4. Chu, Y.I.; Wang, C.M.; Park, J.C.; Lader, P.F. Review of cage and containment tank designs for offshore fish farming. *Aquaculture* **2020**, *519*, 734928. [CrossRef]
5. Ma, C.; Zhao, Y.P.; Bi, C.W. Numerical study on hydrodynamic responses of a single-point moored vessel-shaped floating aquaculture platform in waves. *Aquac. Eng.* **2022**, *96*, 102216. [CrossRef]
6. Wang, G.; Martin, T.; Huang, L.; Bihs, H. A numerical study of the hydrodynamics of an offshore fish farm using REEF3D. *J. Offshore Mech. Arct. Eng.* **2022**, *144*, 021301. [CrossRef]
7. Wang, G.; Martin, T.; Huang, L.; Bihs, H. Numerical investigation of the hydrodynamics of a submersible steel-frame offshore fish farm in regular waves using CFD. *Ocean Eng.* **2022**, *256*, 111528. [CrossRef]
8. Tao, Y.; Zhu, R.; Gu, J.; Wei, Q.; Hu, F.; Xu, X.; Zhang, Z.; Li, Z. Sloshing response of an aquaculture vessel: An experimental study. *J. Mar. Sci. Eng.* **2023**, *11*, 2122. [CrossRef]
9. Kassem, T.; Shahrour, I.; El Khattabi, J.; Raslan, A. Smart and sustainable aquaculture farms. *Sustainability* **2021**, *13*, 10685. [CrossRef]
10. Huang, W.; Zha, R. Numerical studies on internal flow in pipelines of an aquaculture vessel and flow control using a special branch pipe. *Front. Mar. Sci.* **2023**, *10*, 1140285. [CrossRef]
11. Ullah, I.; Kim, D. An optimization scheme for water pump control in smart fish farm with efficient energy consumption. *Processes* **2018**, *6*, 65. [CrossRef]
12. Li, G.; Pan, L.; Hua, Q.; Sun, L.; Lee, K.Y. Water pump control: A hybrid data-driven and model-assisted active disturbance rejection approach. *Water* **2019**, *11*, 1066. [CrossRef]
13. Oca, J.; Masaló, I.; Reig, L. Comparative analysis of flow patterns in aquaculture rectangular tanks with different water inlet characteristics. *Aquac. Eng.* **2004**, *31*, 221–236. [CrossRef]
14. Duarte, S.; Reig, L.; Masaló, I.; Blanco, M.; Oca, J. Influence of tank geometry and flow pattern in fish distribution. *Aquac. Eng.* **2011**, *44*, 48–54. [CrossRef]
15. Oca, J.; Masaló, I. Flow pattern in aquaculture circular tanks: Influence of flow rate, water depth, and water inlet and outlet features. *Aquac. Eng.* **2013**, *52*, 65–72. [CrossRef]
16. Zhao, Y.; Xue, B.; Bi, C.; Ren, X.; Liu, Y. Influence mechanisms of macro-infrastructure on micro-environments in the recirculating aquaculture system and biofloc technology system. *Rev. Aquac.* **2023**, *15*, 991–1009. [CrossRef]
17. Zhang, S.-Y.; Li, G.; Wu, H.-B.; Liu, X.-G.; Yao, Y.-H.; Tao, L.; Liu, H. An integrated recirculating aquaculture system (RAS) for land-based fish farming: The effects on water quality and fish production. *Aquac. Eng.* **2011**, *45*, 93–102. [CrossRef]
18. Campbell, M.D.; Hall, S.G. Hydrodynamic effects on oyster aquaculture systems: A review. *Rev. Aquac.* **2019**, *11*, 896–906. [CrossRef]
19. Che, Z.; Ren, X.; Zhang, Q. Research progress on hydrodynamics in a recirculating aquaculture tank system: A review. *J. Dalian Fish. Univ.* **2021**, *36*, 886–898. [CrossRef]

20. Shi, X.; Li, M.; Huang, Z.; Feng, D.; Ren, X.; Liu, H.; Sun, W. Numerical simulation of the effect of cultured fish on hydrodynamics in an aquaculture tank. *J. Dalian Fish. Univ.* **2023**, *38*, 839–847. [CrossRef]
21. Costa, N.; Maia, R.; Proença, M.; Pinho, F. Edge effects on the flow characteristics in a 90° tee junction. *J. Fluids Eng.* **2006**, *128*, 1204–1217. [CrossRef]
22. Han, F.; Ong, M.C.; Xing, Y.; Li, W. Three-dimensional numerical investigation of laminar flow in blind-tee pipes. *Ocean Eng.* **2020**, *217*, 107962. [CrossRef]
23. Xue, B.; Zhao, Y.; Bi, C.; Cheng, Y.; Ren, X.; Liu, Y. Investigation of flow field and pollutant particle distribution in the aquaculture tank for fish farming based on computational fluid dynamics. *Comput. Electron. Agric.* **2022**, *200*, 107243. [CrossRef]
24. Li, Z.; Guo, X.; Cui, M. Numerical investigation of flow characteristics in a rearing tank aboard an aquaculture vessel. *Aquac. Eng.* **2022**, *98*, 102272. [CrossRef]
25. Anderson, J.D. *Computational Fluid Dynamics: The Basics with Applications*; McGraw-Hill: New York, NY, USA, 1995.
26. Versteeg, H.K.; Malalasekera, W. *An Introduction to Computational Fluid Dynamics: The Finite Volume Method*, 2nd ed.; Pearson Education: Harlow, UK, 2007.
27. Menter, F.R. Two-equation eddy-viscosity turbulence models for engineering applications. *AIAA J.* **1994**, *32*, 1598–1605. [CrossRef]
28. Mockett, C.; Fuchs, M.; Thiele, F. Progress in DES for wall-modelled LES of complex internal flows. *Comput. Fluids* **2012**, *65*, 44–55. [CrossRef]
29. Duraisamy, K.; Iaccarino, G.; Xiao, H. Turbulence modeling in the age of data. *Annu. Rev. Fluid Mech.* **2019**, *51*, 357–377. [CrossRef]
30. Moukalled, F.; Mangani, L.; Darwish, M. *The Finite Volume Method in Computational Fluid Dynamics: An Advanced Introduction with OpenFOAM and MATLAB*; Springer: Cham, Switzerland, 2016. [CrossRef]

Disclaimer/Publisher's Note: The statements, opinions and data contained in all publications are solely those of the individual author(s) and contributor(s) and not of MDPI and/or the editor(s). MDPI and/or the editor(s) disclaim responsibility for any injury to people or property resulting from any ideas, methods, instructions or products referred to in the content.